Search for the neutral Higgs bosons of the MSSM in e^+e^- collisions at $\sqrt{s}$ from 130 to 172 GeV

R. Barate, D. Buskulic, D. Decamp, P. Ghez, C. Goy, J P. Lees, A. Lucotte, M N. Minard, J Y. Nief, B. Pietrzyk, et al.

CERN-PPE/97-071
20 June 1997

Search for the neutral Higgs bosons of the MSSM in e^+e^- collisions at $\sqrt{s}$ from 130 to 172 GeV

The ALEPH Collaboration*)

20 June 1997

Abstract

The process $e^+e^- \to hA$ is used to search for the Higgs bosons of the Minimal Supersymmetric Standard Model (MSSM), in the $b\bar{b}b\bar{b}$ and $\tau^+\tau^- b\bar{b}$ final states. The search is performed in the data collected by the ALEPH experiment at LEP, at centre-of-mass energies between 130 and 172 GeV and with a total luminosity of 27.2 pb^{-1}. No candidate events are found in either of the final states, in agreement with the expected background of 0.91 events from all Standard Model processes. Combined with searches for $e^+e^- \to hZ$, this results in a 95% C.L. lower limit on the masses of both h and A of 62.5 GeV/c^2, for $\tan\beta > 1$.

(Submitted to Physics Letters B)

*) See next pages for the list of authors

The ALEPH Collaboration

R. Barate, D. Buskulic, D. Decamp, P. Ghez, C. Goy, J.-P. Lees, A. Lucotte, M.-N. Minard, J.-Y. Nief, B. Pietrzyk

Laboratoire de Physique des Particules (LAPP), IN^{2}P^3-CNRS, 74019 Annecy-le-Vieux Cedex, France

M.P. Casado, M. Chmeissani, P. Comas, J.M. Crespo, M. Delfino, E. Fernandez, M. Fernandez-Bosman, Ll. Garrido,[15] A. Juste, M. Martinez, G. Merino, R. Miquel, Ll.M. Mir, C. Padilla, I.C. Park, A. Pascual, J.A. Perlas, I. Riu, F. Sanchez, F. Teubert

Institut de Física d'Altes Energies, Universitat Autònoma de Barcelona, 08193 Bellaterra (Barcelona), Spain[7]

A. Colaleo, D. Creanza, M. de Palma, G. Gelao, G. Iaselli, G. Maggi, M. Maggi, N. Marinelli, S. Nuzzo, A. Ranieri, G. Raso, F. Ruggieri, G. Selvaggi, L. Silvestris, P. Tempesta, A. Tricomi,[3] G. Zito

Dipartimento di Fisica, INFN Sezione di Bari, 70126 Bari, Italy

X. Huang, J. Lin, Q. Ouyang, T. Wang, Y. Xie, R. Xu, S. Xue, J. Zhang, L. Zhang, W. Zhao

Institute of High-Energy Physics, Academia Sinica, Beijing, The People's Republic of China[8]

D. Abbaneo, R. Alemany, A.O. Bazarko,[1] U. Becker, P. Bright-Thomas, M. Cattaneo, F. Cerutti, G. Dissertori, H. Drevermann, R.W. Forty, M. Frank, R. Hagelberg, J.B. Hansen, J. Harvey, P. Janot, B. Jost, E. Kneringer, J. Knobloch, I. Lehraus, G. Lutters, P. Mato, A. Minten, L. Moneta, A. Pacheco, J.-F. Pusztaszeri,[20] F. Ranjard, G. Rizzo, L. Rolandi, D. Rousseau, D. Schlatter, M. Schmitt, O. Schneider, W. Tejessy, I.R. Tomalin, H. Wachsmuth, A. Wagner[21]

European Laboratory for Particle Physics (CERN), 1211 Geneva 23, Switzerland

Z. Ajaltouni, A. Barrès, C. Boyer, A. Falvard, C. Ferdi, P. Gay, C . Guicheney, P. Henrard, J. Jousset, B. Michel, S. Monteil, J-C. Montret, D. Pallin, P. Perret, F. Podlyski, J. Proriol, P. Rosnet, J.-M. Rossignol

Laboratoire de Physique Corpusculaire, Université Blaise Pascal, IN^{2}P^3-CNRS, Clermont-Ferrand, 63177 Aubière, France

T. Fearnley, J.D. Hansen, J.R. Hansen, P.H. Hansen, B.S. Nilsson, B. Rensch, A. Wäänänen

Niels Bohr Institute, 2100 Copenhagen, Denmark[9]

G. Daskalakis, A. Kyriakis, C. Markou, E. Simopoulou, A. Vayaki

Nuclear Research Center Demokritos (NRCD), Athens, Greece

A. Blondel, J.C. Brient, F. Machefert, A. Rougé, M. Rumpf, A. Valassi,[6] H. Videau

Laboratoire de Physique Nucléaire et des Hautes Energies, Ecole Polytechnique, IN^{2}P^3-CNRS, 91128 Palaiseau Cedex, France

E. Focardi, G. Parrini, K. Zachariadou

Dipartimento di Fisica, Università di Firenze, INFN Sezione di Firenze, 50125 Firenze, Italy

R. Cavanaugh, M. Corden, C. Georgiopoulos, T. Huehn, D.E. Jaffe

Supercomputer Computations Research Institute, Florida State University, Tallahassee, FL 32306-4052, USA [13,14]

A. Antonelli, G. Bencivenni, G. Bologna,[4] F. Bossi, P. Campana, G. Capon, D. Casper, V. Chiarella, G. Felici, P. Laurelli, G. Mannocchi,[5] F. Murtas, G.P. Murtas, L. Passalacqua, M. Pepe-Altarelli

Laboratori Nazionali dell'INFN (LNF-INFN), 00044 Frascati, Italy

L. Curtis, S.J. Dorris, A.W. Halley, I.G. Knowles, J.G. Lynch, V. O'Shea, C. Raine, J.M. Scarr, K. Smith, P. Teixeira-Dias, A.S. Thompson, E. Thomson, F. Thomson, R.M. Turnbull

Department of Physics and Astronomy, University of Glasgow, Glasgow G12 8QQ,United Kingdom[10]

O. Buchmüller, S. Dhamotharan, C. Geweniger, G. Graefe, P. Hanke, G. Hansper, V. Hepp, E.E. Kluge, A. Putzer, J. Sommer, K. Tittel, S. Werner, M. Wunsch

Institut für Hochenergiephysik, Universität Heidelberg, 69120 Heidelberg, Fed. Rep. of Germany[16]

R. Beuselinck, D.M. Binnie, W. Cameron, P.J. Dornan, M. Girone, S. Goodsir, E.B. Martin, P. Morawitz, A. Moutoussi, J. Nash, J.K. Sedgbeer, P. Spagnolo, A.M. Stacey, M.D. Williams

Department of Physics, Imperial College, London SW7 2BZ, United Kingdom[10]

V.M. Ghete, P. Girtler, D. Kuhn, G. Rudolph

Institut für Experimentalphysik, Universität Innsbruck, 6020 Innsbruck, Austria[18]

A.P. Betteridge, C.K. Bowdery, P. Colrain, G. Crawford, A.J. Finch, F. Foster, G. Hughes, R.W. Jones, T. Sloan, E.P. Whelan, M.I. Williams

Department of Physics, University of Lancaster, Lancaster LA1 4YB, United Kingdom[10]

C. Hoffmann, K. Jakobs, K. Kleinknecht, G. Quast, B. Renk, E. Rohne, H.-G. Sander, P. van Gemmeren, C. Zeitnitz

Institut für Physik, Universität Mainz, 55099 Mainz, Fed. Rep. of Germany[16]

J.J. Aubert, C. Benchouk, A. Bonissent, G. Bujosa, J. Carr, P. Coyle, C. Diaconu, A. Ealet, D. Fouchez, N. Konstantinidis, O. Leroy, F. Motsch, P. Payre, M. Talby, A. Sadouki, M. Thulasidas, A. Tilquin, K. Trabelsi

Centre de Physique des Particules, Faculté des Sciences de Luminy, IN^2P^3-CNRS, 13288 Marseille, France

M. Aleppo, M. Antonelli, F. Ragusa[12]

Dipartimento di Fisica, Università di Milano e INFN Sezione di Milano, 20133 Milano, Italy.

R. Berlich, W. Blum, V. Büscher, H. Dietl, G. Ganis, C. Gotzhein, H. Kroha, G. Lütjens, G. Lutz, W. Männer, H.-G. Moser, R. Richter, A. Rosado-Schlosser, S. Schael, R. Settles, H. Seywerd, R. St. Denis, H. Stenzel, W. Wiedenmann, G. Wolf

Max-Planck-Institut für Physik, Werner-Heisenberg-Institut, 80805 München, Fed. Rep. of Germany[16]

J. Boucrot, O. Callot,[12] S. Chen, A. Cordier, M. Davier, L. Duflot, J.-F. Grivaz, Ph. Heusse, A. Höcker, A. Jacholkowska, M. Jacquet, M. Kado, D.W. Kim,[2] F. Le Diberder, J. Lefrançois, A.-M. Lutz, I. Nikolic, M.-H. Schune, L. Serin, S. Simion, E. Tournefier, J.-J. Veillet, I. Videau, D. Zerwas

Laboratoire de l'Accélérateur Linéaire, Université de Paris-Sud, IN^2P^3-CNRS, 91405 Orsay Cedex, France

P. Azzurri, G. Bagliesi, S. Bettarini, C. Bozzi, G. Calderini, V. Ciulli, R. Dell'Orso, R. Fantechi, I. Ferrante, A. Giassi, A. Gregorio, F. Ligabue, A. Lusiani, P.S. Marrocchesi, A. Messineo, F. Palla, G. Sanguinetti, A. Sciabà, J. Steinberger, R. Tenchini, C. Vannini, A. Venturi, P.G. Verdini

Dipartimento di Fisica dell'Università, INFN Sezione di Pisa, e Scuola Normale Superiore, 56010 Pisa, Italy

G.A. Blair, L.M. Bryant, J.T. Chambers, Y. Gao, M.G. Green, T. Medcalf, P. Perrodo, J.A. Strong, J.H. von Wimmersperg-Toeller

Department of Physics, Royal Holloway & Bedford New College, University of London, Surrey TW20 OEX, United Kingdom[10]

D.R. Botterill, R.W. Clifft, T.R. Edgecock, S. Haywood, P. Maley, P.R. Norton, J.C. Thompson, A.E. Wright

Particle Physics Dept., Rutherford Appleton Laboratory, Chilton, Didcot, Oxon OX11 OQX, United Kingdom[10]

B. Bloch-Devaux, P. Colas, B. Fabbro, W. Kozanecki, E. Lançon, M.C. Lemaire, E. Locci, P. Perez, J. Rander, J.-F. Renardy, A. Rosowsky, A. Roussarie, J.-P. Schuller, J. Schwindling, A. Trabelsi, B. Vallage

CEA, DAPNIA/Service de Physique des Particules, CE-Saclay, 91191 Gif-sur-Yvette Cedex, France[17]

S.N. Black, J.H. Dann, H.Y. Kim, A.M. Litke, M.A. McNeil, G. Taylor

Institute for Particle Physics, University of California at Santa Cruz, Santa Cruz, CA 95064, USA[19]

C.N. Booth, R. Boswell, C.A.J. Brew, S. Cartwright, F. Combley, M.S. Kelly, M. Lehto, W.M. Newton, J. Reeve, L.F. Thompson

Department of Physics, University of Sheffield, Sheffield S3 7RH, United Kingdom[10]

K. Affholderbach, A. Böhrer, S. Brandt, G. Cowan, J. Foss, C. Grupen, P. Saraiva, L. Smolik, F. Stephan

Fachbereich Physik, Universität Siegen, 57068 Siegen, Fed. Rep. of Germany[16]

M. Apollonio, L. Bosisio, R. Della Marina, G. Giannini, B. Gobbo, G. Musolino

Dipartimento di Fisica, Università di Trieste e INFN Sezione di Trieste, 34127 Trieste, Italy

J. Putz, J. Rothberg, S. Wasserbaech, R.W. Williams

Experimental Elementary Particle Physics, University of Washington, WA 98195 Seattle, U.S.A.

S.R. Armstrong, E. Charles, P. Elmer, D.P.S. Ferguson, S. González, T.C. Greening, O.J. Hayes, H. Hu, S. Jin, P.A. McNamara III, J.M. Nachtman, J. Nielsen, W. Orejudos, Y.B. Pan, Y. Saadi, I.J. Scott, J. Walsh, Sau Lan Wu, X. Wu, J.M. Yamartino, G. Zobernig

Department of Physics, University of Wisconsin, Madison, WI 53706, USA[11]

[1] Now at Princeton University, Princeton, NJ 08544, U.S.A.

[2] Permanent address: Kangnung National University, Kangnung, Korea.

[3] Also at Dipartimento di Fisica, INFN Sezione di Catania, Catania, Italy.

[4] Also Istituto di Fisica Generale, Università di Torino, Torino, Italy.

[5] Also Istituto di Cosmo-Geofisica del C.N.R., Torino, Italy.

[6] Supported by the Commission of the European Communities, contract ERBCHBICT941234.

[7] Supported by CICYT, Spain.

[8] Supported by the National Science Foundation of China.

[9] Supported by the Danish Natural Science Research Council.

[10] Supported by the UK Particle Physics and Astronomy Research Council.

[11] Supported by the US Department of Energy, grant DE-FG0295-ER40896.

[12] Also at CERN, 1211 Geneva 23,Switzerland.

[13] Supported by the US Department of Energy, contract DE-FG05-92ER40742.

[14] Supported by the US Department of Energy, contract DE-FC05-85ER250000.

[15] Permanent address: Universitat de Barcelona, 08208 Barcelona, Spain.

[16] Supported by the Bundesministerium für Bildung, Wissenschaft, Forschung und Technologie, Fed. Rep. of Germany.

[17] Supported by the Direction des Sciences de la Matière, C.E.A.

[18] Supported by Fonds zur Förderung der wissenschaftlichen Forschung, Austria.

[19] Supported by the US Department of Energy, grant DE-FG03-92ER40689.

[20] Now at School of Operations Research and Industrial Engireering, Cornell University, Ithaca, NY 14853-3801, U.S.A.

[21] Now at Schweizerischer Bankverein, Basel, Switzerland.

1 Introduction

In minimal extensions of the Standard Model, two Higgs doublets are introduced in order to give masses to up-type quarks and down-type quarks separately. In these models, the Higgs sector therefore consists of five physical states, namely three neutral bosons — two CP-even h and H, and one CP-odd A — and a pair of charged bosons $H^{\pm}$. Six independent parameters are required: four Higgs boson masses, the ratio $v_2/v_1 \equiv \tan\beta$ of the vacuum expectation values of the two Higgs doublets, and α, the mixing angle in the CP-even sector.

Predictions can therefore only be made in specific models, of which the most popular is the Minimal Supersymmetric extension of the Standard Model (MSSM). In this model, both H and $H^{\pm}$ are predicted to be too heavy to be discovered at LEP 2. The analysis presented in this letter is consequently restricted to the search for the lighter Higgs bosons, h and A, which can be produced by two complementary processes, the Higgs-strahlung process $e^+e^- \to hZ$ with a cross section proportional to $\sin^2(\beta-\alpha)$ and the associated pair-production $e^+e^- \to hA$ with cross section proportional to $\cos^2(\beta-\alpha)$. In Fig. 1 the hA cross section is shown for the LEP 1 energy of 91 GeV and the three LEP 2 energies: 133, 161 and 172 GeV.

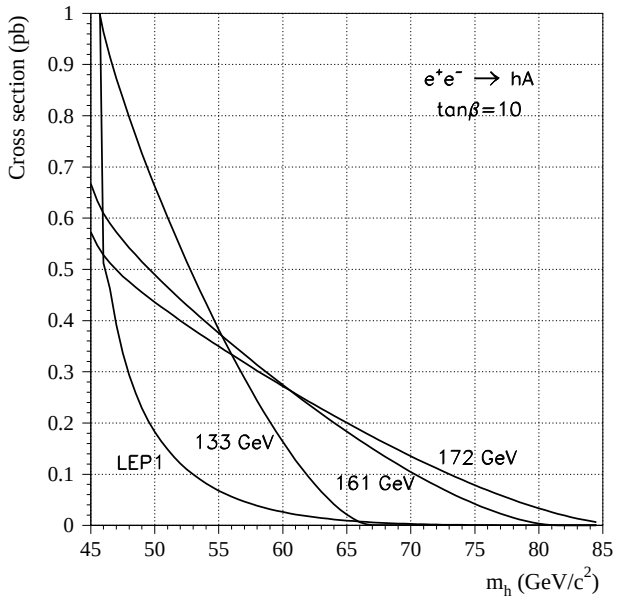

Figure 1: The cross section for associated production $e^+e^- \to hA$ at LEP 1 and the three LEP 2 energies used in the analysis.

At tree-level, only two parameters are needed to determine all the other relevant quantities (masses, couplings, and therefore cross sections). Here, these are chosen to be $\tan\beta$ and the mass m_h. When radiative corrections are included at the one [1] and two [2] loop levels, three other parameters are needed, namely M_{SUSY}, A_t and μ. In the stop sector, the overall mass scale is characterised by M_{SUSY} and the mixing is controlled by A_t and μ. In this letter the results are presented for $M_{SUSY} = 1\,\mathrm{TeV}/c^2$ and for two extreme configurations of stop mixing:

no mixing ($A_t,\ \mu \ll M_{SUSY}$) and maximal mixing ($A_t - \mu/\tan\beta = \sqrt{6}\,M_{SUSY}$), as suggested in [3]. The latter leads to the largest radiative correction to m_h and is therefore the most pessimistic choice for LEP, while the first is the most optimistic. Varying M_{SUSY} from 0.2 to 5 TeV/c^2 does not change the basic conclusions of this letter.

The analyses described in this letter search for associated hA production in data collected with the ALEPH detector at LEP at $\sqrt{s}$ from 130 to 172 GeV during the years 1995 and 1996. For $m_h = 60\,\mathrm{GeV}/c^2$ and $\tan\beta$ =10 the branching fraction of h and A to $b\overline{b}$ is 92% and to $\tau^+\tau^-$ is 8%, giving $b\overline{b}b\overline{b}$ final states in 84% of the events and $\tau^+\tau^- b\overline{b}$ in 14%. Analyses of both these channels are performed. After describing the relevant aspects of the ALEPH detector in Section 2, the method used for tagging the b quark jets is described in Section 3. The event selections, detailed in Section 4, are optimized for $m_h = m_A = 60\,\mathrm{GeV}/c^2$ with the procedure described in [4], using the reconstructed mass sum $m_h + m_A$ as the discriminating variable. In Section 5, the results from the hA modes of this letter are combined with the hZ modes of [4] and results are presented within the MSSM as a function of $\sin^2(\beta-\alpha)$ and as a function of $\tan\beta$.

2 The ALEPH detector

The ALEPH detector and its performance are described in [5] and [6]. In October 1995, the silicon vertex detector (VDET) described in these papers was replaced by a new device [7] which is used for the analyses described herein. This new VDET is twice as long as the previous detector, providing a larger acceptance and has less material in the active region.

With this modification the tracking system consists of the VDET, with two layers at average radii 6.3 and 11.0 cm measuring coordinates with a resolution of 12 μm in the rϕ dimension and 15-50 μm in the z dimension for incident angles between 0° and 70°, surrounded by the inner tracking chamber (ITC) and the time projection chamber (TPC). Charged particles are used in the analyses if they are reconstructed with at least four hits in the TPC (typically corresponding to a polar angle with respect to the beam $|\cos\theta| < 0.96$) and they originate from within a cylinder of length 20 cm and a radius of 2 cm coaxial with the beam and centered at the interaction point. Tracks with $|\cos\theta| < 0.94$ (0.85) pass through at least one (two) layer(s) of the new VDET. The resulting three dimensional impact parameter resolution can be parametrized as $(34 + 70/p)(1 + 1.6\cos^4\theta)$ μm (p in GeV/c). With the axial magnetic field of 1.5T the momentum resolution of the tracking system is given by $\sigma(p)/p = 6 \times 10^{-4} p_T \oplus 0.005$ (p_T in GeV/c). The TPC provides up to 338 measurements of the specific ionization, $\mathrm{d}E/\mathrm{d}x$, on the tracks.

The tracking chambers are surrounded by a lead/proportional-chamber electromagnetic calorimeter (ECAL) and a hadron calorimeter (HCAL) consisting of the iron magnet return yoke instrumented with streamer tubes. With two external streamer chamber layers the HCAL is also used for muon identification. The ECAL and HCAL have relative energy resolutions of $0.18/\sqrt{E} + 0.009$ and $0.85/\sqrt{E}$ (E in GeV). The calorimetry and tracking information are combined in an energy flow algorithm [6] which gives a measure of the total energy, and therefore the missing energy, with an error of $(0.6\sqrt{E} + 0.6)$ GeV. The various neutral particles

reconstructed from the calorimeters together with the charged particle tracks used in this algorithm are referred to as "energy flow particles".

Lepton identification in ALEPH is described in [6, 8]. Electrons are identified by comparing the energy deposit in the ECAL with the momentum measured in the tracking system, the shape and depth of the energy deposit in the ECAL and the specific ionization measurement. Muons are identified by requiring a hit pattern characteristic of a penetrating particle in the HCAL and at least one associated hit in the muon chambers. In all analyses described in this letter electron and muon candidates must have momenta greater than 2 GeV/c and 3 GeV/c, respectively.

3 b tagging

For the analyses of both the $\mathrm{b\overline{b}b\overline{b}}$ and $\tau^+\tau^-\mathrm{b\overline{b}}$ channels the b quark identification is an essential part of the signal extraction. In this letter b jets are identified mainly by exploiting the longer lifetime of b hadrons compared to other hadrons, but also by the presence in the jets of high p_T leptons from semileptonic decays. To use the lifetime information in a given jet, track impact parameters and secondary decay vertices are reconstructed relative to an event-by-event interaction point.

3.1 Interaction point determination

The algorithm used to determine the interaction point is similar to the one developed for the data taken at centre-of-mass energies close to the Z mass [9]. Well measured tracks are associated to their nearest jet and are projected into the plane perpendicular to this jet, to reduce the bias due to tracks coming from secondary vertices. The projected tracks are then combined with an average "beam spot" position, *i.e.*, the location of the centre of the interaction region in the plane transverse to the beam axis. This beam spot is determined with relaxed cuts on the track selection compared to LEP 1 due to the much lower track rate at LEP 2 energies. Using groups of 120 tracks selected in consecutive events and with momenta down to 300 MeV/c, the beam spot position is determined with average accuracies of $\sim$27μm in the horizontal and $\sim$25μm in the vertical directions. The RMS dimensions of the beam luminous region were measured to be 135 (150) μm horizontally and 7.1 (6.6) mm along the beam direction in the 1995 (1996) data. The vertical dimension of the luminous region is small, of order 5 μm. Using these parameters as errors on the beam spot, the interaction point is found in each event with resolutions of typically 40, 20 and 40 μm in the horizontal, vertical and beam directions.

3.2 b tagging neural network

Six variables which discriminate between b jets and light quark jets are combined using neural networks to tag b quark jets. The first two variables are lifetime-based; the third is based

on the transverse momentum of identified leptons and the last three are based on jet-shape properties. The quantities used are as follows:

1. $\mathcal{P}_{\rm jet}$: probability of the jet being a light quark (uds) jet based upon impact parameters of tracks in the jet, similar to that described in Ref. [9] with modifications for the new VDET;

2. $\Delta\chi^2_{\rm svx}$: the χ^2 difference between fitting tracks in the jet both to secondary and primary vertices compared to assuming all tracks come from the interaction point. This is based upon a secondary vertex pattern recognition algorithm which searches for displaced vertices via a three-dimensional grid point search [10];

3. $p_{\rm T}$: the transverse momentum of identified leptons with respect to the jet axis [8];

4. $\mathcal{S}^{\rm b}$: the boosted sphericity of the jet, defined to be the sphericity of energy flow particles in the rest frame of the jet;

5. Multiplicity/ln$E_{\rm jet}$: the energy flow particle multiplicity of the jet divided by the logarithm of the jet energy. Normalizing by ln$E$ removes the expected energy dependence of the multiplicity;

6. $\Sigma p_{\rm T}^2$: the sum of the transverse momentum squared of each energy flow particle with respect to the jet axis.

For the hA analysis, a neural network based upon the first three variables ($\mathcal{P}_{\rm jet}$, $\Delta\chi^2_{\rm svx}$, and $p_{\rm T}$) is used for identifying b-jets while all six variables are used in another neural network for the Higgs-strahlung process [4]. In this latter analysis, the extra variables which are efficient at discriminating between b-jets and light quark jets give higher b tagging efficiency at a given background; in the hA case, however, the six-variable neural network increases the background of bbgg events due to the similarity between gluon and b jets in the event shape variables [11].

The network architecture is multilayer feed-forward, consisting of four layers and is based upon the JETNET 3.4 package [12]. Detailed descriptions of theoretical aspects of neural networks are available elsewhere [13]. The neural network was trained, with the backward propagation method, using b and non-b jets in radiative returns to the Z from a sample of 400,000 Monte Carlo q$\bar{\rm q}$ events generated at a centre-of-mass energy of 161 GeV. Radiative returns to the Z were used because the jets in such events are produced in a kinematic configuration similar to that of the signal; this was preferred to training the network using simulated signal events in order to reduce the associated systematic error in the signal efficiency.

An independent sample of 100,000 Monte Carlo events was used for testing. The resulting neural network output is shown in Fig. 2a for jets in the 161 GeV data and Monte Carlo, selected using the Durham jet finding algorithm with $y_{cut} = 0.008$. For events in the testing sample, it is possible to determine the efficiency for identifying b jets, $\epsilon_{\rm b}^{\rm jet}$, as a function of the rejection for non-b jets, $(1-\epsilon_{\rm udscg}^{\rm jet})$, where $\epsilon_{\rm udscg}^{\rm jet}$ is the efficiency for wrongly identifying a light quark or gluon jet as a b jet. The resulting performance curve is shown in Fig. 2b; the curve for the single most powerful variable $\mathcal{P}_{\rm jet}$ is also given, showing at a non-b rejection factor of 85% a gain in b efficiency from 78% to 87% by combining the extra information in the neural network.

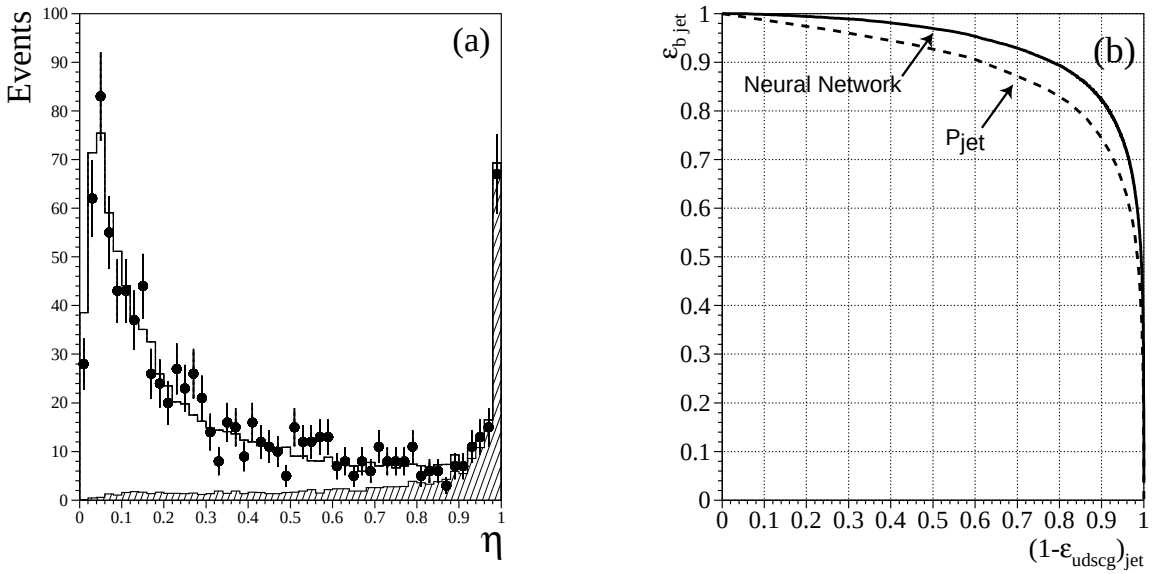

Figure 2: (a) The output η of the neural network b tag for radiative returns to the Z for 161 GeV $q\bar{q}$ Monte Carlo (histogram) compared to the data at 161 GeV (points). The shaded region shows the contribution from generated b-jets. (b) The performance of the neural network b tag (solid line) for Monte Carlo events, presented in terms of the efficiency for identifying b-jets versus the efficiency for rejecting light quark jets. The performance of the single most powerful b tagging input variable to the neural network is shown for comparison (dashed curve).

3.3 Systematic studies of b tagging

The systematic uncertainty in the efficiency of the b tagging is evaluated from the Monte Carlo simulation and a consistency check is performed on efficiency and background using the calibration data taken at the Z peak during the 1996 data taking period.

The contribution to the b tagging systematics from the physics of b hadron decays has been estimated by varying the values of their lifetimes and decay multiplicities within the range allowed by existing experimental measurements [14]. The systematics due to track reconstruction have been studied by comparing track impact parameter distributions in data and Monte Carlo. The generated Monte Carlo distributions show impact parameter resolutions 10% better than in the data. A correction has been applied for this effect by smearing the track parameters in the Monte Carlo to calculate the analysis efficiency and half this correction is taken as a systematic error in the b tag efficiency.

After this correction is applied, the b tag efficiency is compared in Monte Carlo and data at the Z peak, by measuring the number of events with two and one hemispheres tagged by the algorithm. This method is a simplified version of that used to measure $R_{\rm b}$ in Ref. [9]. In that paper the equations for the number of double and single tags are solved to eliminate the b tag efficiency and extract $R_{\rm b}$; here the value of $R_{\rm b}$ is input and the b tag efficiency is

extracted. Figure 3 shows the resulting comparison of the b tag efficiency as a function of the neural network output for one jet. Data and Monte Carlo agree within the statistical errors.

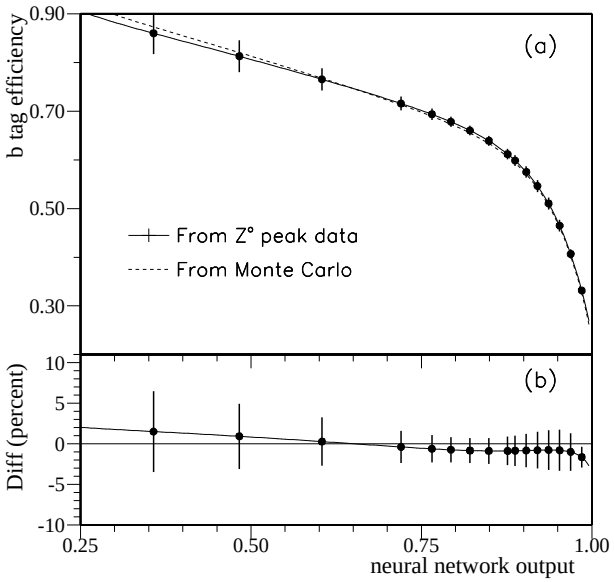

Figure 3: Comparison of the neural network b tag efficiency for a single jet in Z peak data and Monte Carlo, after the smearing correction, as a function of the cut on the jet neural network output: (a) absolute tag efficiency; (b) difference between data and Monte Carlo.

4 Event selection

The data samples used in these analyses comprise $5.7\,\mathrm{pb}^{-1}$ at energies of $\sqrt{s} = 130.2$ and 136.2 GeV recorded in November 1995, $10.9\,\mathrm{pb}^{-1}$ at 161.3 GeV in the summer of 1996, $1.1\,\mathrm{pb}^{-1}$ at 170.3 GeV and $9.5\,\mathrm{pb}^{-1}$ at 172.3 GeV in autumn 1996. The new VDET was completely installed for the 1996 data while for the November 1995 data the inner layer of the detector was complete but 5 out of 15 faces were missing in the outer layer. The appropriate detector geometries were used in the Monte Carlo for the two years.

For cut optimization and background estimates Monte Carlo samples were generated using the HZHA [15] program for the Higgs signal production and PYTHIA 5.7 [16] for the standard process production. The backgrounds considered are described in Ref. [4].

4.1 The $\mathrm{b\bar{b}b\bar{b}}$ final state

The $\mathrm{b\bar{b}b\bar{b}}$ final state is characterized by two clear signatures, the four-jet topology and a high b-quark content. These properties are the main handles for suppressing the background. The main source of background is the two fermion process $\mathrm{e^+e^-} \to \mathrm{q\bar{q}}(\gamma)$, predominantly when the

two primary partons are b quarks. At the higher centre-of-mass energies, two more processes, WW and ZZ (including $Z\gamma^*$) production, also become significant.

The first step in the analysis is a loose preselection intended to select hadronic events compatible with the four-jet topology and to suppress $q\bar{q}\gamma$ events with an energetic initial state radiation (ISR) photon. At least eight charged particles are required in the event comprising more than 10% of the centre-of-mass energy. To reject $q\bar{q}\gamma$ events with the ISR photon detected in the calorimeters, the electromagnetic energy in a cone of 1° around each energy flow particle in any jet must be less than 80% of the jet energy. To suppress these events when the photon escapes detection along the beam pipe, the missing longitudinal momentum is required to be less than $1.5 \times (M_{\rm vis} - 90)$, where $M_{\rm vis}$ (in GeV/c^2) is the total visible mass in the event. The events are then clustered into four jets using the Durham algorithm. Events with y_{34}, the maximum $y_{\rm cut}$ value giving a four-jet event, smaller than 0.001 are rejected. The event thrust must be less than 0.85 and the smallest jet-jet angle, $\theta_{ij}^{\rm min}$, must be larger than 20°. The signal efficiency is 87% for $b\bar{b}b\bar{b}$ events at this level, while the $q\bar{q}$ background is reduced by a factor of ~ 40, the ZZ by a factor of almost 10 and the WW by more than 2. A total of 208 events are observed in the data, in agreement with the 188 events (112 $q\bar{q}$, 67 WW, 9 ZZ) predicted by the simulation. The excess of four-jet events reported in a previous paper [17] is present at this level of the analysis, but none of these events remain after the b tagging cut applied next.

The final selection combines the b tagging information in the event and a measure of compatibility with the four-jet topology. The b tagging variable uses the neural network outputs, η_j (described in the previous section), from all four jets, j, in the form

$$\mathcal{B}_4 = 4 - \sum_{j=1}^{4} \eta_j \,,$$

while for the four-jet compatibility $\theta_{ij}^{\rm min}$ was chosen. These were combined linearly in a new variable $\mathcal{F}$:

$$\mathcal{F} = 90 \times \mathcal{B}_4 - \theta_{ij}^{\rm min} \quad (\ \theta_{ij}^{\rm min} \text{ in degrees}) \,.$$

The choice of the coefficient of $\mathcal{F}$ was made with a linear discriminant analysis and the separation of signal and background is indicated in Fig. 4. Combining the b tag and four-jet compatibility information improves significantly the signal efficiency, compared to cutting independently on the individual variables, by saving some clear four-jet events with poorer b tagging information as well as some events with high content in b quarks but where two of the jets happen to be close in space.

The cut on $\mathcal{F}$ was placed at the point that minimizes the expected confidence level in the absence of signal, for the hypothesis $m_{\rm h} = m_{\rm A} = 60\,{\rm GeV}/c^2$ [4]. This optimization procedure gave $\mathcal{F} < 49$, which corresponds to a signal efficiency of 55% at 172 GeV centre-of-mass energy. Figure 7b shows the signal efficiencies for the three energies as a function of $m_{\rm h}$. The distribution of $\mathcal{F}$ in the data and in the simulation is shown in Fig. 5a. For $\mathcal{F} < 49$, 0.87 ± 0.17 events (0.63 $q\bar{q}$, 0.07 WW, 0.17 ZZ) are expected in the simulation. No events were selected in the data. Fig. 5b shows distributions of the reconstructed signal mass sum $m_{\rm h} + m_{\rm A}$ which has been used as the discriminating variable in the cut optimization. This quantity is the sum of dijet masses for the pairing of jets with the minimum dijet mass difference and uses jet energies rescaled with the beam energy constraint [17].

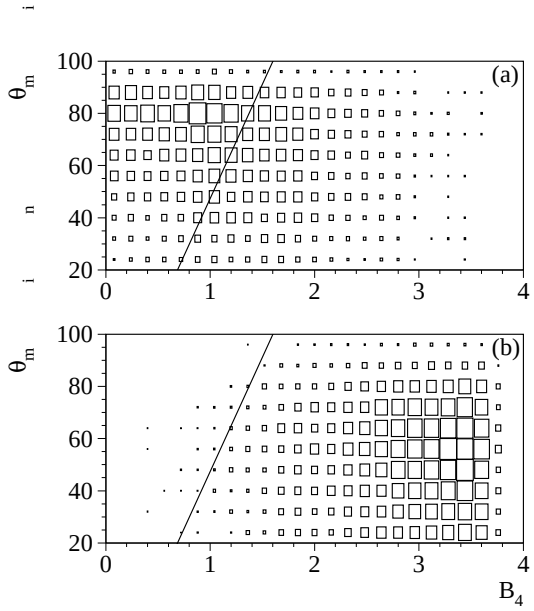

Figure 4: Monte Carlo distribution of the minimum angle between jets $\theta_{ij}^{\rm min}$ versus the b tagging variable $\mathcal{B}_4$ (a) for the signal hA events, (b) for the background, $q\bar{q}$, WW and ZZ events. The line indicates the cut described in the text.

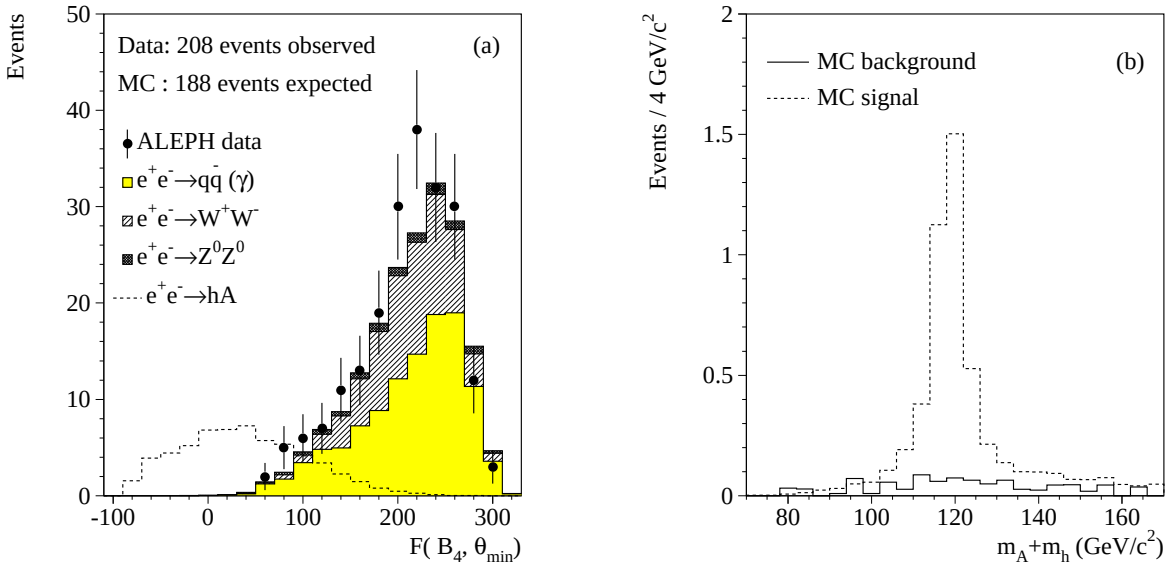

Figure 5: (a) Distribution of data after the $b\bar{b}b\bar{b}$ preselection cuts at all energies as a function of the variable $\mathcal{F}(\mathcal{B}_4, \theta_{ij}^{\rm min})$ described in the text. The background predictions from the Monte Carlo simulations are shown as cumulative shaded histograms and the dashed histogram is the signal for a luminosity $10\times$ that in the data. (b) Distribution of mass sum $m_{\rm h} + m_{\rm A}$ for signal and background Monte Carlo events, normalized to the recorded luminosity, after all cuts.

The b tagging cut, bringing the major loss in signal acceptance, gives the largest systematic uncertainty in the analysis efficiency. The b hadron lifetimes were varied within the ranges given by current world averages [18] by reweighting the generated hA signal Monte Carlo, giving a systematic error on the $b\overline{b}b\overline{b}$ efficiency of 0.7%. The systematics from other b physics sources are estimated to be 0.4%. The accuracy of the correction to the track resolution described in Section 3.3 is estimated from the comparison shown in Fig. 3 and a systematic of 0.8% is assigned to the efficiency, corresponding to 50% of the change due to the correction. With a contribution of 0.5% for Monte Carlo statistics the total systematic error is 1.2%. This is propagated to the final results using the method of Ref. [19] and changes the limits by negligible amounts.

4.2 The $\tau^+\tau^-b\overline{b}$ final state

The $\tau^+\tau^-b\overline{b}$ final state is selected by two complementary approaches. In the first approach, the tau decay products are first identified using charged particle tracks and tau candidates are constructed by the inclusion of neutral clusters in a cone around these tracks. In the second method, events are first clustered into four jets and jets consistent with tau decays are selected. In the following the first and second methods are referred to respectively as "track-based" and "jet-based".

4.2.1 Track-based selection

A preselection is first applied which selects high multiplicity hadronic final states and which rejects radiative returns to the Z peak. Hadronic events are selected by requiring at least ten charged particles which account for at least 20% of the centre-of-mass energy. Radiative returns with undetected photons down the beam axis are rejected by requiring the longitudinal missing momentum to be less than 30 GeV/c. The signal events are also characterized by missing energy and transverse momentum imbalance due to the undetected neutrinos. This is exploited by requiring the missing energy to be larger than 5 GeV and the momentum imbalance in the plane transverse to the beam axis to be larger than 5 GeV/c.

Tau leptons are identified by searching for identified electrons and muons, single charged particles and charged particle triplets with differing isolation requirements. To avoid the large potential contamination from background processes involving energetic leptons (e.g., eeZ, ZZ and WW), events with identified leptons with momenta larger than 40 GeV/c are rejected. Lepton candidates are required to be isolated by more than 10° using the isolation definition of the $H\ell^+\ell^-$ channel described in Ref. [4]. Identified leptons which do not pass these criteria are not considered for the purposes of tau selection. The remaining tracks are rejected as tau candidates if another track falls within 10°. Charged particle triplets are identified by considering all combinations which have unit net charge and where no track except the three under consideration falls within 10° of the resultant vector. In all cases candidates with a net charged momentum less than 2 GeV/c are no longer considered. Tau candidates are constructed by adding the four-momenta of all the energy flow particles within 15° of the tau tracks. Tau candidates with a momentum less than 3 GeV/c or with a mass larger than 1.8 GeV/c^2 are

rejected.

In events with an identified lepton, background from W pair events is rejected by reconstructing the event as $\mathrm{WW} \to \mathrm{qq}\ell\nu$, where the missing four-momentum in the event is assigned to the neutrino and the remaining energy flow particles are assigned to the other W. Events in which the mass sum of the reconstructed W's is greater than $140\,\mathrm{GeV}/c^2$ and the mass of the hadronically-decaying W is less than $85\,\mathrm{GeV}/c^2$ are rejected.

Events are required to have at least two tau candidates of opposite charge, and at least one of the tau jets is required to have unit charged multiplicity. The sum of the isolation angles of the tau candidates is required to be larger than 80°. Energy flow particles not included in the tau jets are clustered into two jets using the Durham algorithm.

A fit is performed on the event, where the four jet directions are fixed to the measured ones and the jet momenta are determined from the fit. The masses of the tau jets are constrained to the nominal tau mass. The other two jets are rescaled keeping their velocities fixed to the measured values. The fit minimizes a χ^2 with contributions from energy-momentum conservation, the mass difference of the two dijet systems (in accordance with the $m_\mathrm{A} \approx m_\mathrm{h}$ hypothesis) and the estimated uncertainties on the measurements of the non-tau jets. In the fit the tau jet momenta are constrained to be larger than 90% of the measured values. Combinations in which either of the fitted values for the non-tau jet momenta is less than 75% of the measured energy are no longer considered. The distribution of χ^2 for the signal and background Monte Carlo is shown in Fig. 6a. Combinations with $\chi^2 > 20$ are rejected. If more than one combination passes the selection criteria, the combination with the smallest χ^2 is kept. In signal events the resolution on the tau dijet mass using this method is about $3\,\mathrm{GeV}/c^2$. The fitted mass of the tau pair is required to lie between $40\,\mathrm{GeV}/c^2$ and $70\,\mathrm{GeV}/c^2$.

The background is further reduced by means of the three-input neural network b tag. A requirement is placed on the sum of the outputs for the two non-tau jets, using an optimization procedure [4] which minimizes the expected confidence level of the $\mathrm{b\overline{b}b\overline{b}}$ analysis combined with that of the $\tau^+\tau^-\mathrm{b\overline{b}}$ analysis. The b tagging variable defined as

$$\mathcal{B}_2 = 2 - \sum_{i=1}^{2} \eta_i$$

is required to be smaller than 1.15.

Based on Monte Carlo simulation, the expected background is 0.02 ± 0.01 event. The efficiency to select $m_\mathrm{A} \approx m_\mathrm{h} \approx 60\,\mathrm{GeV}/c^2$ is 32% at 172 GeV and similar at 161 GeV.

4.2.2 Jet-based selection

Hadronic events are selected by requiring at least eight charged particles which account for more than 10% of the centre-of-mass energy. The longitudinal momentum of the event is required to be less than $40\,\mathrm{GeV}/c$, the reconstructed missing energy is required to be positive, and the transverse momentum must be larger than $5\,\mathrm{GeV}/c$. Events in which the thrust is greater than 0.9 are rejected.

The Durham algorithm is used to cluster the event into four jets, and the y_{34} value is

required to be greater than 0.001. All four jets are required to contain at least one charged particle, and at least one jet must have less than seven energy flow particles.

The two lowest multiplicity jets are considered for tau selection. Only charged particles with momenta above $1\,\mathrm{GeV}/c$ are used in the following to select tau candidates. For these jets the total momentum of the charged particles is required to be larger than $2\,\mathrm{GeV}/c$, and the mass of each jet must be less than $1.8\,\mathrm{GeV}/c^2$.

The charged multiplicity of one of the tau candidates must be unity, and the sum of the charged multiplicities of the two jets is required to be six or less. The sum of the charges of the two tau candidates is required to be zero.

The four jets are fitted in the same way as for the track-based selection. The χ^2 of the fit, Fig. 6b, is required to be less than 20, and the reconstructed mass of the di-tau system must fall in the same mass range as for the track-based analysis. The same three-input neural network b tag is used, requiring $\mathcal{B}_2 < 0.85$. The cut is optimized to minimize the expected combined confidence level of the $\mathrm{b\overline{b}b\overline{b}}$, track-based and jet-based analyses.

From the Monte Carlo simulation, the expected background is 0.02 ± 0.01 events. The selection efficiency for $m_\mathrm{A} \approx m_\mathrm{h} \approx 60\,\mathrm{GeV}/c^2$ is 30% at 172 GeV and 27% at 161 GeV.

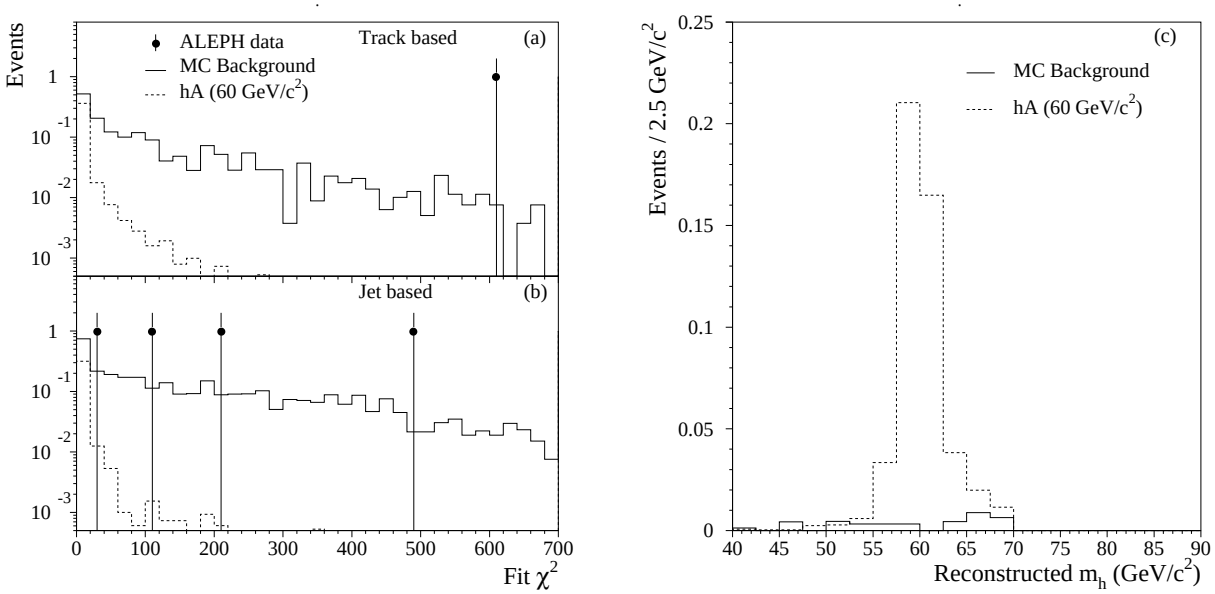

Figure 6: The fit χ^2 variable in the $\tau^+\tau^-\mathrm{b\overline{b}}$ (a) track-based and (b) jet-based analyses with all cuts except those on the b tagging variable. The points are the data, the solid histogram is the total background prediction from the simulations and the dashed histogram is the expectation from $m_\mathrm{A} \approx m_\mathrm{h} \approx 60\,\mathrm{GeV}/c^2$ for a luminosity corresponding to the data. (c) Reconstructed mass m_h in the combined $\tau^+\tau^-\mathrm{b\overline{b}}$ analysis for signal and background after all cuts.

4.2.3 Combined $\tau^+\tau^-\mathrm{b\overline{b}}$ selection

The track-based and the jet-based analyses are combined by selecting events if they pass at least one of the selections. The overlap between the two selections for the signal is around 60%, with almost no common background. Fig. 6c shows the reconstructed m_h distribution for the

signal and background. The final efficiency for the $\tau^+\tau^-\mathrm{b\bar{b}}$ combined selection is $\sim 45\%$ for $m_\mathrm{A} \approx m_\mathrm{h} \approx 60\,\mathrm{GeV}/c^2$ and is shown in Fig. 7c as a function of mass and centre-of-mass energy. The expected background is 0.04 ± 0.02 events. No candidates are observed by either analysis.

The two principal systematic uncertainties are common to the two $\tau^+\tau^-\mathrm{b\bar{b}}$ analyses: the energy flow reconstruction and the b tagging. Uncertainties on the efficiency can occur due to the simulation of reconstructed energy flow particles which can affect the efficiency of the cut on the χ^2 of the mass fit. The fit is recalculated with non-tau jet energies smeared within their errors. The effect is very small and gives a difference on signal efficiencies less than 0.2%. The b tagging effects are studied using a similar approach as for the $\mathrm{b\bar{b}b\bar{b}}$ channel. Reweighting generated signal events with different b hadron lifetimes changes the efficiency by less than 0.3% and the systematic due to the correction to the track resolution is evaluated to be 0.3%. Systematics are dominated by the 1.1% uncertainty due to Monte Carlo statistics. Adding all these effects in quadrature gives a total systematic error of 1.2% which has a negligible impact on the final result.

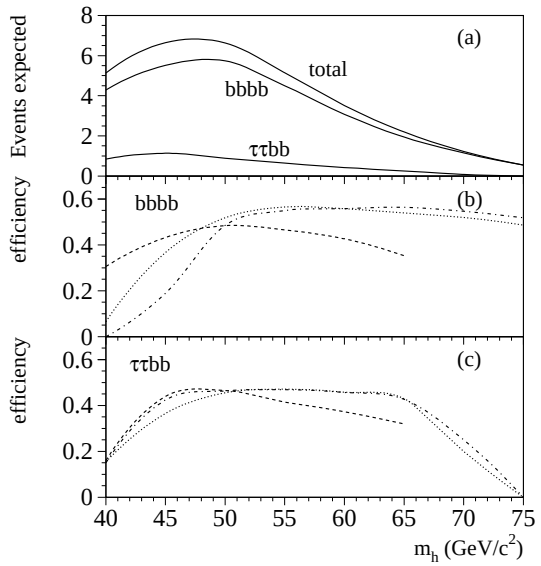

Figure 7: Shown for $\tan\beta = 10$, where $m_\mathrm{A} \approx m_\mathrm{h}$, as a function of mass: (a) Expected number of events for the two channels and the total. (b) Efficiency for the $\mathrm{b\bar{b}b\bar{b}}$ channel for the three energies: 133 GeV dashed, 161 GeV dotted, 172 GeV dot-dashed. (c) Efficiencies for $\tau^+\tau^-\mathrm{b\bar{b}}$ channel for the three energies.

5 Combined results of hA and hZ analyses

No candidate events were retained by any of the selections presented in the previous sections, in agreement with the 0.91 ± 0.17 events expected from Standard Model processes. The results of the two selections were combined together, and then combined with the result of the search for the Higgs-strahlung process $\mathrm{e^+e^-} \to \mathrm{hZ}$ [4], in the following way [20].

First, the measured and expected confidence levels were computed both for the $\mathrm{b\bar{b}b\bar{b}}$ and the $\tau^+\tau^-\mathrm{b\bar{b}}$ final states, from the numbers of events expected from Standard Model processes and from signal (with $\cos^2(\beta-\alpha)=1$), using the reconstructed mass sum $m_\mathrm{h}+m_\mathrm{A}$ as discriminating variable. Since no candidate events have been selected, the measured confidence level is simply $\exp(-s)$, where s is the number of events from signal expected to be selected by each analysis (shown in Fig. 7a). The expected combined confidence level is displayed with the measured individual and combined confidence levels in Fig. 8a.

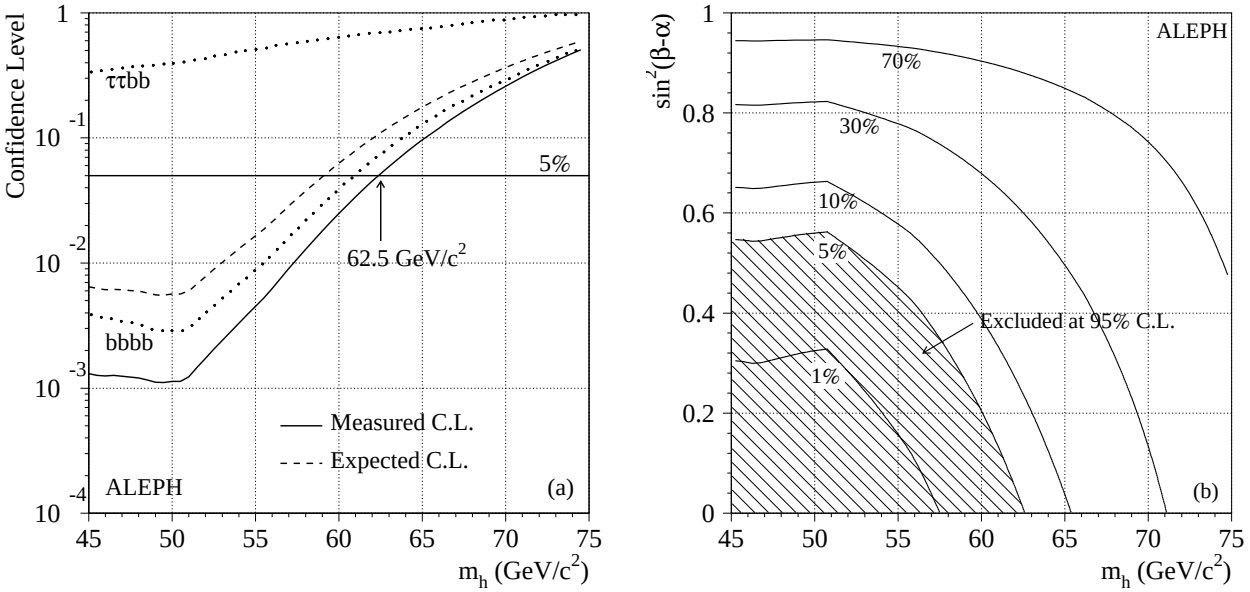

Figure 8: (a) Measured confidence levels as a function of m_h (dotted curves) for the two final states produced by the $\mathrm{e^+e^-}\to\mathrm{hA}$ process, and for their combination (solid curve). Also shown is the combined expected confidence level (dashed curve). (b) Measured confidence level in the $m_\mathrm{h}, \sin^2(\beta-\alpha)$ plane, obtained from the combined $\mathrm{e^+e^-}\to\mathrm{hA}$ search.

As a result of this combination, the m_h range between 45 and 62.5 GeV/c^2 is excluded at more than 95% C.L. for $\cos^2(\beta-\alpha)=1$, *i.e.*, in a region of the MSSM parameter space in which $m_\mathrm{h}=m_\mathrm{A}$ and the decay branching ratios of h and A into $\mathrm{b\bar{b}}$ and $\tau^+\tau^-$ are largest. The mass range below 45 GeV/c^2 was already excluded at much more than 95% C.L. by LEP 1 analyses [21, 22]. The same operation was repeated varying $\cos^2(\beta-\alpha)$ from 1 to 0. The resulting confidence level curves are shown in Fig. 8b in the $[m_\mathrm{h}, \sin^2(\beta-\alpha)]$ plane.

When $\cos^2(\beta-\alpha)$ becomes too small for the $\mathrm{e^+e^-}\to\mathrm{hA}$ searches to contribute, $\sin^2(\beta-\alpha)$ becomes large enough for $\mathrm{e^+e^-}\to\mathrm{hZ}$ searches [4] to play a significant rôle. The confidence level presented in Ref. [4] was therefore derived again by varying $\sin^2(\beta-\alpha)$ from unity (its value in the Standard Model) to zero. The resulting confidence level curves are shown in Fig. 9a in the $[m_\mathrm{h}, \sin^2(\beta-\alpha)]$ plane.

Finally, the confidence levels obtained in the $[m_\mathrm{h}, \sin^2(\beta-\alpha)]$ plane by the hZ and hA searches were combined. The result is displayed in Fig. 9b. All values of m_h below 62.5 GeV/c^2 can be excluded at more than 95% C.L.

These confidence levels in the $[m_\mathrm{h}, \sin^2(\beta-\alpha)]$ plane can be translated into a 95% C.L.

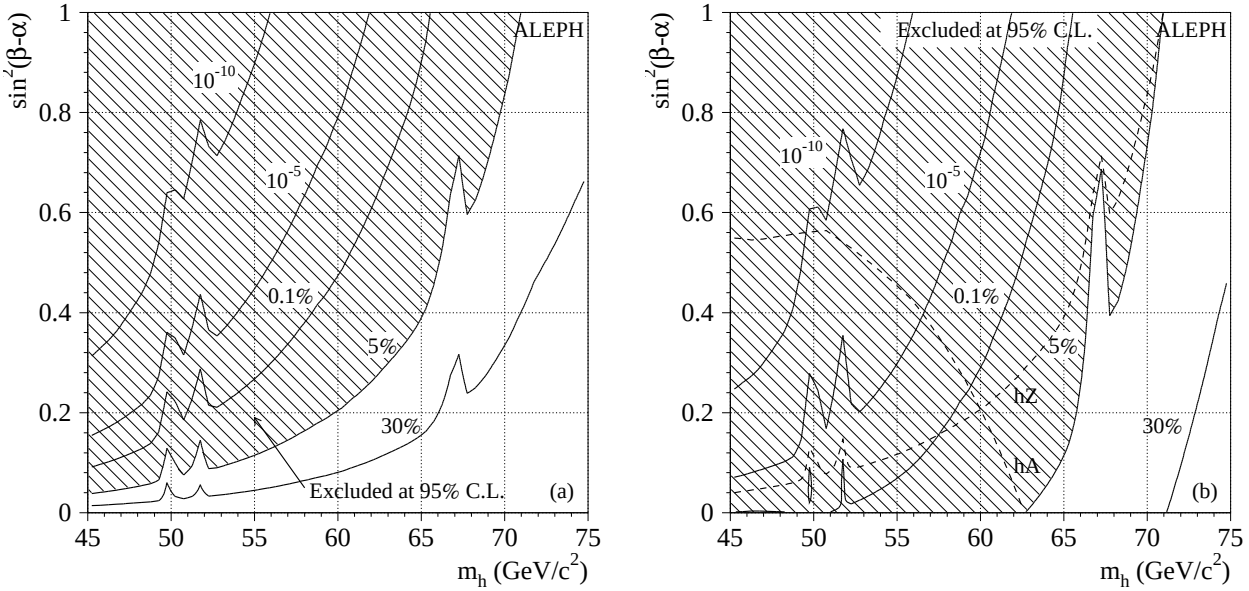

Figure 9: Measured confidence levels in the $[m_{\mathrm{h}}, \sin^2(\beta-\alpha)]$ plane (a) from $\mathrm{e^+e^-} \to \mathrm{hZ}$ searches, and (b) from the combination of $\mathrm{e^+e^-} \to \mathrm{hZ}$ and hA (solid curves) and again the 5% confidence levels for the hA and hZ analyses separately (dashed curves).

excluded region in the usual $[m_{\mathrm{h}}, \tan\beta]$ plane, as shown in Fig. 10. The heavily shaded regions, theoretically not allowed, depend on the choice of parameters for stop mixing and on the top quark mass. (A value of 175 GeV/c^2 [23] was used.) The experimentally excluded region is, however, identical in both cases of no mixing and maximal mixing.

When varying $\cos^2(\beta-\alpha)$, the hA production cross section was modified accordingly, but neither the m_{A} value nor the h and A branching fractions (and therefore hA selection efficiencies) were changed from their values at $\cos^2(\beta-\alpha) = 1$. However, the hA analysis efficiencies have been checked to be unchanged at the level of 1% for mass differences of h and A below 10 GeV/c^2. With the choices of MSSM parameters given in Section 1, this is always the case when the $\mathrm{e^+e^-} \to \mathrm{hA}$ cross section is not vanishingly small. The h and A branching ratio variations have also been found to have a negligible effect.

The same holds true for hZ when varying $\sin^2(\beta-\alpha)$, except when m_{A} is small enough for the $\mathrm{h} \to \mathrm{AA}$ decay to occur. When $m_{\mathrm{A}} > 2m_{\mathrm{b}}$, however, A mostly decays into $\mathrm{b\bar{b}}$ (and h into $\mathrm{b\bar{b}b\bar{b}}$). This renders the hZ selections of Ref. [4] at least as efficient as when h decays into $\mathrm{b\bar{b}}$ and the limits are conservative. This is no longer the case when $m_{\mathrm{A}} < 2m_{\mathrm{b}}$. This case must be dealt with by means of separate selections and is not addressed in this letter. Since such a light A has already been excluded by dedicated $\mathrm{e^+e^-} \to \mathrm{hZ^*/hA}$ searches at LEP 1 [21] for m_{h} values below $\sim$ 60 GeV/c^2, the region corresponding to this configuration is a strip too narrow to be visible in Fig. 10, close to the theoretically forbidden domain and affecting only the $\tan\beta < 1$ region.

The invisible decay $\mathrm{h} \to \chi\chi$ could also affect the validity of the result if the lightest neutralino χ were light enough. This possibility is excluded by the negative chargino searches performed at LEP 1.5 [24], when the GUT mass relations between charginos and neutralinos

are satisfied [25].

To conclude, if the search is restricted to theoretically favoured $\tan\beta$ values in excess of unity, both m_{h} and m_{A} must be larger than 62.5 GeV/c^2 at the 95% confidence level.

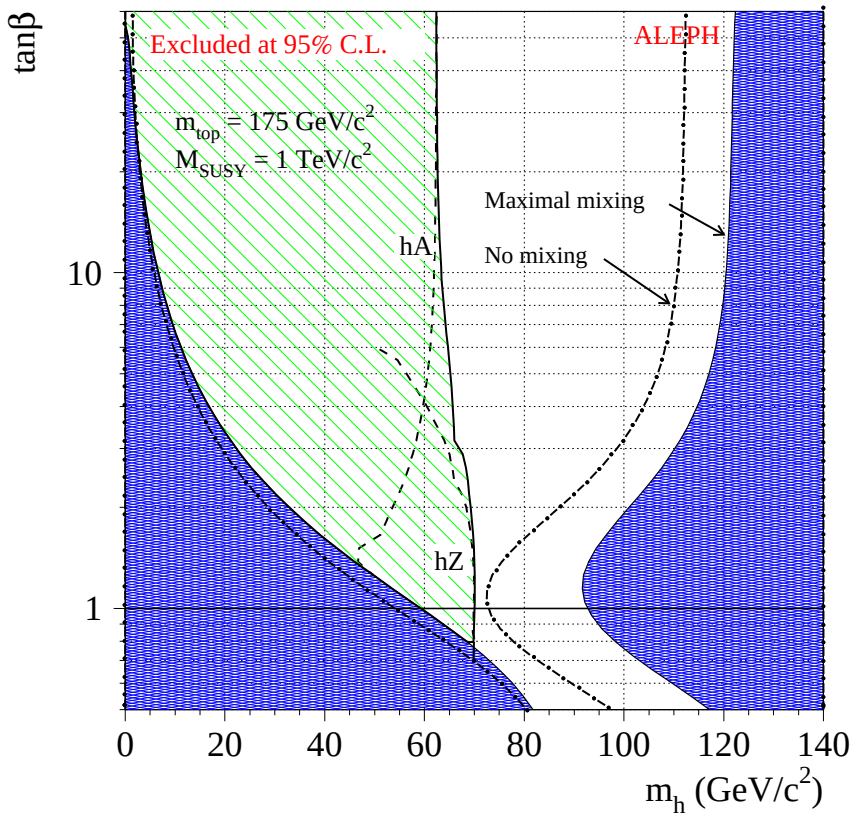

Figure 10: The [m_{h},$\tan\beta$] plane in the maximal mixing configuration. The dark areas are theoretically disallowed. The hatched area is excluded at the 95% confidence level by the combined search for $\mathrm{e^+e^-} \to \mathrm{hZ}$ and $\mathrm{e^+e^-} \to \mathrm{hA}$. The dot-dashed lines show the change in the theoretically excluded region in the no mixing configuration.

6 Conclusions

A search has been made for the neutral Higgs bosons h and A of the Minimal Supersymmetric Standard Model using a total of 27.2 pb^{-1} of data collected at centre-of-mass energies from 130 to 172 GeV. For the associated production $\mathrm{e^+e^-} \to \mathrm{hA}$, searches have been performed in the $\mathrm{b\bar{b}b\bar{b}}$ and $\tau^+\tau^-\mathrm{b\bar{b}}$ final states. No candidate events were found in either channel with a total background expectation of 0.91 ± 0.17. This result was combined with the results reported in Ref. [4] on the search for $\mathrm{e^+e^-} \to \mathrm{hZ}$ to give exclusion limits on m_{h} as a function of $\sin^2(\beta-\alpha)$ and as a function of $\tan\beta$ for typical sets of MSSM parameters. For values of $\tan\beta > 1$, h and A are excluded for masses less than 62.5 GeV/c^2 at 95% confidence level.

Acknowledgements

We wish to thank our colleagues from the accelerator divisions for the successful operation of LEP at high energy. We are indebted to the engineers and technicians in all our institutions for their contribution to the excellent performance of ALEPH. Those of us from non-member countries thank CERN for its hospitality.

References

[1] Y. Okada, M. Yamaguchi and T. Yanagida, *Progr. Theor. Phys.* **85** (1991) 1;
J. Ellis, G. Ridolfi and F. Zwirner, *Phys. Lett.* **B257** (1991) 83; **B262**(1991) 477;
H.E. Haber and R. Hempfling, *Phys. Rev. Lett.* **66** (1991) 1815;
R. Barbieri, M. Frigeni and F. Caravaglios, *Phys. Lett.* **B258** (1991) 167;
R. Barbieri and M. Frigeni, *Phys. Lett.* **B258** (1991) 395.

[2] M. Carena, M. Quiros, C.E.M. Wagner, *Nucl. Phys.* **B461** (1996) 407;
M. Carena, J.R. Espinosa, M. Quiros and C.E.M. Wagner, *Phys. Lett.* **B355** (1995) 209;
H. E. Haber, R. Hempfling and A. H. Hoang, CERN-TH-95-216 (1995).

[3] M. Carena, P.M. Zerwas (Conveners) et al. , "*Higgs Physics*", in Physics at LEP 2, Ed. G. Altarelli, T. Sjöstrand and F. Zwirner, CERN 96-01 (1996) 351.

[4] ALEPH Collaboration, "*Search for the Standard Model Higgs Boson at* $\sqrt{s}$ *=161, 170 and 172 GeV*", CERN PPE-97-070, submitted to *Physics Letters B.*

[5] ALEPH Collaboration, *Nucl. Instrum. Methods* **A294** (1990) 121;
B. Mours et al., *Nucl. Instrum. Methods* **A379** (1996) 101.

[6] ALEPH Collaboration, *Nucl. Instrum. Methods* **A360** (1995) 481.

[7] "*Construction and Performance of the new ALEPH Vertex Detector*", D. Creanza et al., to appear in the Proceedings of the 5th International Conference on Advanced Technology and Particle Physics, Como, Italy, October 1996.

[8] ALEPH Collaboration, *Nucl. Instrum. Methods* **A346** (1994) 461.

[9] ALEPH Collaboration, *Phys. Lett.* **B313** (1993) 535.

[10] ALEPH Collaboration, *Phys. Lett.* **B322** (1994) 441.

[11] ALEPH Collaboration, *Phys. Lett.* **B384** (1996) 353.

[12] L. Lönnblad, C. Peterson, and T. Rögnvaldsson, CERN-TH.7135/94.

[13] C. Peterson and T. Rögnvaldsson, *1991 CERN School of Computing* (Ed. C. Verkerk) 113;
L. Lönnblad, C. Peterson, and T. Rögnvaldsson, *Comp. Phys. Comm.* **70** (1992) 167;
S.R. Amendolia, *1993 CERN School of Computing* (Eds. C. E. Vandoni and C. Verkerk) 1.

[14] ALEPH, DELPHI, L3 and OPAL Collaborations, *Nucl. Instrum. Methods* **A378** (1996) 101.

[15] P. Janot, "*The HZHA generator*", in Physics at LEP 2, Eds. G Altarelli, T. Sjöstrand and F. Zwirner, CERN 96-01 (1996) 309.

[16] T. Sjöstrand, "*The PYTHIA 5.7 and JETSET 7.4 Manual*", LU-TP.95/20 and CERN-TH.7112/93.

[17] ALEPH Collaboration, *Z. Phys.* **C71** (1996) 179.

[18] Particle Data Group, *Phys. Rev.* **D54** (1996) 1.

[19] R.D. Cousins and V.L. Highland, *Nucl. Instrum. Methods* **A320** (1992) 331.

[20] P. Janot and F. Le Diberder, *" Combining 'Limits' "*, CERN/PPE 97-053, LPNHE/97-01, to be submitted to *Nucl. Instrum. Methods.*

[21] ALEPH Collaboration, *Phys. Rep.* **216** (1992) 253; *Phys. Lett.* **B285** (1992) 309; **B313**(1993) 312; **B384**(1996) 427;
DELPHI Collaboration, *Z. Phys.* **C67** (1995) 69; *Nucl. Phys.* **B421** (1994) 3;
OPAL Collaboration, *Z. Phys.* **C73** (1997) 189;
L3 Collaboration, *Z. Phys.* **C57** (1993) 355; *Phys. Lett.* **B385** (1996) 454.

[22] P. Janot, "*Searching for Higgs bosons at LEP 1 and LEP 2*", to appear in Perspectives on Higgs Physics II, World Scientific, ed. G.L. Kane.

[23] J. Lys (for CDF Collaboration), S. Protopopescu (for D0 Collaboration) and P. Tipton, talks given at ICHEP96, Warsaw, 25-31 July 1996, to appear in the proceedings.

[24] ALEPH Collaboration, *Phys. Lett.* **B373** (1996) 246.

[25] A. Djouadi, P. Janot, J. Kalinowski and P.M. Zerwas, *Phys. Lett.* **B376** (1996) 220.